Supporting Information for

An 'ice-like' water film for corrosion-proof seawater electrolysis

Zihui Yuan, [a] Yingxia Zhao,[d]* Yue Sun,[a] Yingying Xu,[a] Yuanhong Zhong,[a] Shaomin Peng,[a] Ming Sun,[a],[c],[e] Ning Yan,[f] Youwen Liu,[b],[g]* and Lin Yu[a], [e]*

[a] Z. Yuan, Y Sun, Y. Xu, Prof. Y. Zhong, Prof. S. Peng Prof. M. Sun, Prof. L. Yu
GuangDong Engineering Technology Research Center of Modern Fine Chemical Engineering, School of Chemical Engineering and Light Industry, Guangdong University of Technology, Guangzhou, 510006, China
E-mail: gych@gdut.edu.cn

[b] Prof. Y. Liu
State Key Laboratory of Materials Processing and Die & Mould Technology, and School of Materials Science and Engineering, Huazhong University of Science and Technology, Wuhan, Hubei, 430074, China.
E-mail: ywliu@hust.edu.cn

[c] Prof. M. Sun
Jieyang Branch of Chemistry and Chemical Engineering Guangdong Laboratory (Rongjiang Laboratory), Jieyang, 515200, China
E-mail: sunmgz@gdut.edu.cn

[d] Y. X. Zhao
Analysis and Test Center Guangdong University of Technology, Guangdong University of Technology, Guangzhou, 510006, China

[e] Prof. M. Sun
Guangdong Yuntao Hydrogen Energy Technology Co., Ltd, Guangzhou, 551040, China

[f] N. Yan
Key Laboratory of Artificial Micro, and Nano-structures of Ministry of Education, School of Physics and Technology, Wuhan University, Wuhan 430072, China

[g] Prof. Y. Liu
Research Institute of Huazhong University of Science and Technology in Shenzhen, Shenzhen, 518057 P. R. China.

Experimental section

Materials:

Cobalt(II) nitrate hexahydrate ($Co(NO_3)_2·6H_2O$, >99%), nickel(II) nitrate hexahydrate ($Ni(NO_3)_2·6H_2O$, >99%), iridium(IV) oxide (IrO_2, >99%), and potassium hydroxide (KOH, >90%) were purchased from Aladdin Chemical Reagent Co., Ltd. Iron(II) sulfate heptahydrate ($FeSO_4·7H_2O$, >99%), sodium hypophosphite monohydrate ($NaH_2PO_2·H2O$, >99%), sodium acetate (CH_3COONa, >99%), and ammonium sulfate ($(NH_4)_2SO_4$, >99%) were obtained from Guangzhou Chemical Reagent Factory. Platinum on carbon (Pt/C, 20 wt.%) was purchased from Shanghai Macklin Biochemical Co., Ltd. Nickel foam (thickness: 0.3 mm, porosity: 97.2%) was acquired from Tianjin Aweixin Chemical Technology Co., Ltd. All chemicals were of analytical grade and used without further purification.

Synthesis of CNFPO and CNFO self-supported catalytic electrodes：

The CNFPO designation used throughout the text refers to the cobalt-nickel-iron layered oxide/hydroxide with phosphate doping. For clarity and comparative purposes, the control catalyst is designated as CNFO, representing the cobalt-nickel-iron layered double oxide/hydroxide.

The CNFPO and CNFO self-supported catalysts loaded on nickel foam were synthesized via a one-step electrodeposition method. First, the nickel foam substrate was pretreated by ultrasonically cleaning in 3 M HCl, ethanol, and deionized water for 10 minutes each. Subsequently, a homogeneous solution was prepared by dissolving 1 mmol $Co(NO_3)_2·6H_2O$, 1 mmol $Ni(NO_3)_2·6H_2O$, 1 mmol $FeSO_4·7H_2O$, 18 mmol $NaH_2PO_2·H_2O$, 25 mmol $(NH_4)_2SO_4$, and 1 mmol CH_3COONa in 100 mL of deionized water. The pH of the solution was adjusted to 2 using 3 M H_2SO_4, followed by magnetic stirring for 15 minutes.

The electrodeposition of CNFPO was carried out in a three-electrode system, where the cleaned nickel foam, an Ag/AgCl electrode, and a carbon rod served as the working electrode, reference electrode, and counter electrode, respectively. Chronoamperometric electrodeposition was performed at a potential of -1.8 V vs. Ag/AgCl for 13 minutes. After washing with ultrapure water and drying at 60 °C for 3 hours, the CNFPO electrode was

obtained. The control sample, CNFO, was synthesized using the same procedure but without the addition of $NaH_2PO_2 \cdot H_2O$.

Characterization:

The X-ray diffraction (XRD) analysis to characterize the physical structure. X-ray diffraction (XRD) patterns were collected on a PANalytical （X'Pert3 Powder）Advance diffractometer using Cu Kα radiation (λ = 1.5406 Å) operating at 40 kV and 40 mA. Data were recorded in the 2θ range of 10–80° with a scan rate of 2° min^{-1} and a step size of 0.02°.The morphological evaluations were observed through the utilization of a scanning electron microscope (SEM, ZEISS, SUPRA 55) and transmission electron microscope (TEM, JEOL JEM-2200FS) equipped with X-ray energy spectroscopy (EDS). The Raman spectra were studied on laser confocal Raman spectroscopy (HORIBA Jobin Yvon, LabRAM HR Evolution) using a 532 nm laser as an excitation source. XPS analysis was performed using a Thermo Fisher Escalab 250Xi instrument to analyse the elemental valence states of the materials using C 1s (binding energy of 285 eV) as a reference. TOF-SIMS surface analysis was carried out using the instrument ION-TOF. TOF-SIMS which was used to obtain information on the chemical composition and morphology of the material surface. A UV photoelectron spectrometer (UPS) model Escalab 250Xi, Thermo Fisher, UK was used to react the work function (WF) of the materials.

Potential-dependent in situ Raman spectroscopy

Raman spectra were acquired using a HORIBA Jobin Yvon LabRAM HR Evolution confocal Raman microscope equipped with a 532 nm excitation laser. The spectrometer was configured with a 600 lines mm^{-1} grating, providing a spectral resolution of approximately 1.5 cm^{-1}. The Raman signal was collected in backscattering geometry through a 50× long working distance objective (NA = 0.5). Each spectrum represents an accumulation of 3 acquisitions with an acquisition time of 5 seconds per scan. Calibration was performed using the 520.7 cm^{-1} line of a silicon standard prior to each measurement session. For operando measurements, a custom-built electrochemical cell with a quartz window was employed, and spectra were collected at each applied potential after a 5-minute stabilization period. A custom electrochemical cell with a circular quartz glass

window was used to protect the objective lens. The working electrode was positioned perpendicular to the incident laser, while a carbon rod and Ag/AgCl electrode served as the counter and reference electrodes, respectively. Deionized water in the electrolyte was replaced with deuterium oxide (D_2O) for KOH dissolution.

DFT calculations

Spin-polarized electronic structure calculations were performed using the plane-wave basis set approach as implemented in the Vienna ab initio simulation package (VASP)[1]. The projector augmented wave (PAW) method was used to represent the ion–core electron interactions[2]. The valence electrons were represented with a plane wave basis set with an energy cutoff of 450 eV. Electronic exchange and correlation were described with the Perdew–Burke–Ernzerhof (PBE) functional[3] DFT-D3 method was used to treat the van der Waals interaction[4]. 15 Å vacuum space was included to avoid interactions between surface slabs. A 3×3×1 Monkhorst–Pack scheme was used to generate the k-point grid for the modeled surfaces[5]. The convergence criteria for the self-consistent electronic structure and geometry were set to 10−5 eV and 0.05 eV/Å, respectively. Zero-point vibrational energy (ZPVE) corrections are calculated by assuming a quantum harmonic oscillator possessing the calculated vibrational frequency.

Molecular dynamics simulations

Molecular dynamics (MD) simulations were conducted using the Forcite module with the Universal force field in Materials Studio[6]. Van der Waals and Coulomb interactions were considered, using atom-based and Ewald methods with a 12.5 Å cutoff. The motion equations were integrated at a 1 fs time step. Following energy minimization, each system underwent a 100 ps relaxation period under periodic boundary conditions in the NPT ensemble (Pressure = 1 atmosphere, Temperature = 298.0 K), using the Nose thermostat and Berendsen barostat for stabilization of temperature, potential, and total energy. After equilibrium, a 500-ps simulation in the NVT ensemble was performed for trajectory analysis, radial distribution function (RDF), and coordinate number (CN) analysis.

we use the same notation of "1 M H_2O" and "10 M H_2O" in Figure 1e to represent low and high water concentration conditions, respectively. chloride ions (Cl^-) were directly

introduced into the computational model to examine their interactions with water molecules and the catalyst surface, making it unnecessary to define the system as NaCl solution.

Electrochemical tests

All electrochemical tests in this paper were carried out using a Zahner Zennium electrochemical workstation and a three-electrode test system from Zahner, Germany, in which graphite rods, Ag/AgCl (3.5 M KCl, 0.2046 V vs. RHE), and monolithic samples (1 × 1 cm^2 exposed area) were used as counter electrode, reference electrode, and working electrode, respectively. For electrolytes, 1.0 M KOH, 1.0 M KOH +0.5 M NaCl, and 1.0 M KOH + real seawater (1 M KOH + seawater electrolyte was prepared by dissolving solid KOH in natural seawater (including ~0.5 M NaCl), followed by 5 h of precipitation of the precipitates and adjusting the pH value to 14 (± 0.2) were selected, respectively. As alkaline water, alkaline simulated seawater, and alkaline real seawater electrolytes. The electrolytes were purged with N_2 for 30 minutes to achieve saturation. Catalysts were electrochemically activated before testing, and potentials were converted to the reversible hydrogen electrode (RHE) scale using the Nernst equation:

$$E_{RHE} = E\,(Ag/AgCl) + 0.059 \cdot pH + 0.1989$$

Cyclic voltammetry (CV) was performed for 30 cycles at a scan rate of 100 mV s^{-1} between -0.6 and 0 V vs. RHE for activation. Linear sweep voltammetry (LSV) curves were recorded at a scan rate of 5 mV s^{-1}. Electrochemical impedance spectroscopy (EIS) was conducted in the frequency range of 10^{-1} to 10^5 Hz. Double-layer capacitance (Cdl) values were calculated from CV curves obtained at scan rates of 20–100 mV s^{-1}. Stability tests were performed using chronopotentiometry at 50 mA cm^{-2}.

AEM membrane electrode testing

For AEM water electrolyzer measurements, titanium felt (Ti) was used as the substrate for both the anode (CoFe-LDH) and cathode (CNFPO). The electrolyzer was assembled with spacers, CoFe-LDH, an anion exchange membrane (AEM, PiperION A40), CNFPO@Ti, and spacers. The cell was operated at room temperature with a peristaltic pump circulating 1.0 M KOH + 0.5 M NaCl simulated seawater electrolyte at a

flow rate of 10 mL min^{-1}. AEM electrolyzer tests were conducted using a CHI660E electrochemical workstation. For temperature-dependent measurements, the sealed electrolyte glass cell was immersed in a thermostatic water bath for heating.

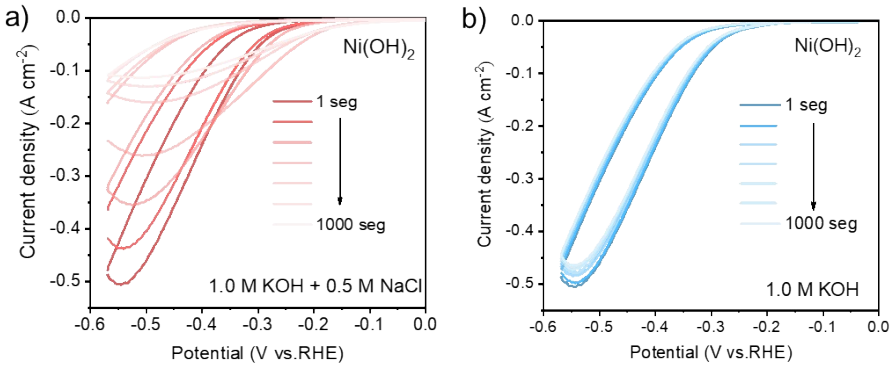

Figure S1. CV curve of $Ni(OH)_2$ in alkaline simulated seawater and 1 M KOH. The NaCl-free electrolyte shows substantially smaller current decay and no obvious pitting morphology compared with NaCl-containing simulated seawater. This control experiment confirms that while the catalyst itself exhibits good intrinsic stability, the presence of chloride ions substantially accelerates deactivation under these operating conditions.

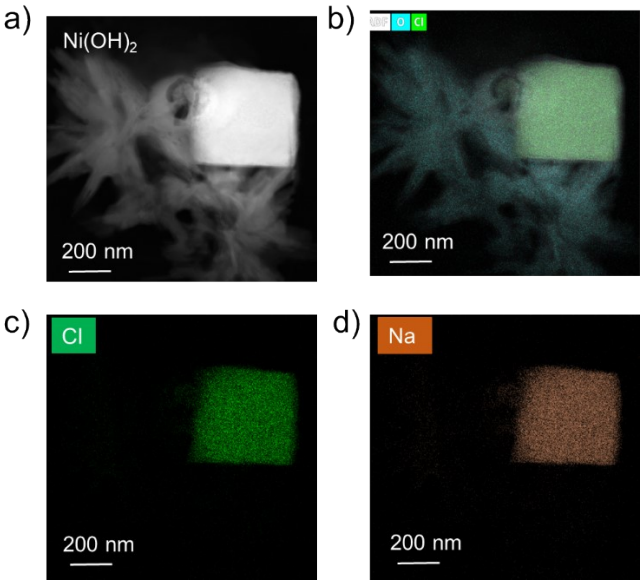

Figure S2. The EDS elemental mapping image of the sample after CV cycling. the primary constituents are sodium (Na) and chlorine (Cl).

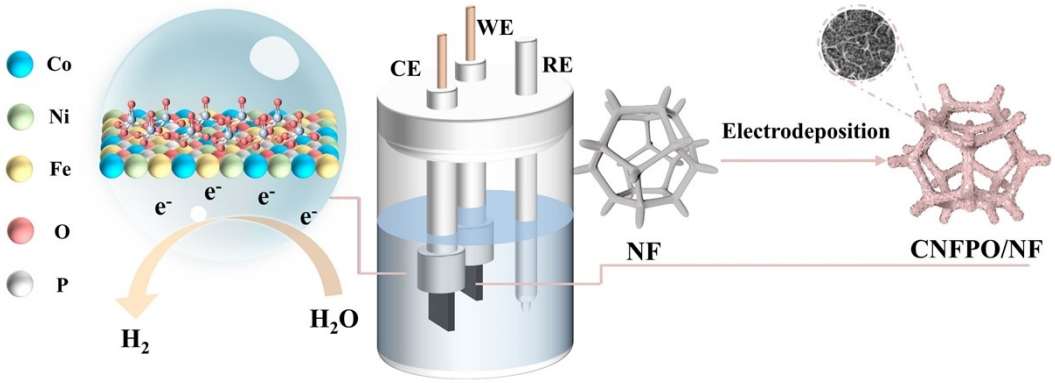

Figure S3. Schematic illustration of the CNFPO synthesis. The CNFPO self-supported catalyst on nickel foam was rapidly fabricated via an in situ electrochemical atomic deposition method. Unlike gas-phase or solvothermal routes, the electroplating approach offers rapid preparation under ambient temperature and pressure. The CNFPO or CNFO catalyst was obtained by electroplating with or without sodium hypophosphite in the electrolyte. The applied potential (−1.8 V vs Ag/AgCl) is lower than the standard reduction potentials (E^o) of the involved reactions, ensuring their occurrence:

$$Ni^{2+} + 2e^- \rightarrow Ni \quad (E^o = -0.25 \text{ V vs SHE})$$

$$Co^{2+} + 2e^- \rightarrow Co \quad (E^o = -0.28 \text{ V vs SHE})$$

$$Fe^{2+} + 2e^- \rightarrow Fe \quad (E^o = -0.44 \text{ V vs SHE})$$

$$H_2PO_2^- + e^- + 2H^+ \rightarrow P + 2H_2O \quad (E^o \approx -0.50 \text{ V vs SHE})$$

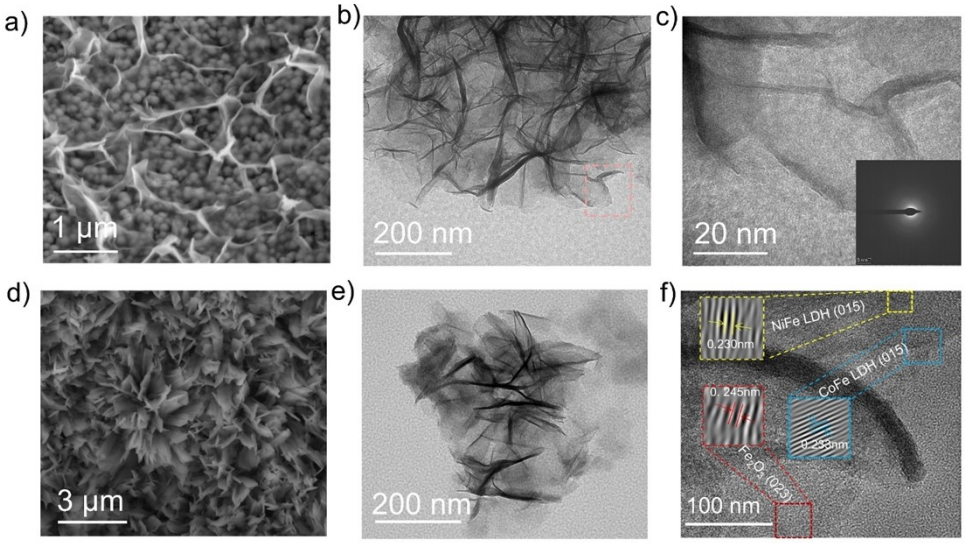

Figure S4. Morphological characterization of CNFPO and CNFO catalysts. SEM, TEM, HR-TEM and the corresponding SADE images (insets). (a-c) CNFPO. (d-f) CNFO. The surface of CNFPO is covered with randomly shaped nanosheets (Supplementary Figure S2a). In contrast to CNFO (Figure S2d and S2e), which exhibits nanosheets with lateral dimensions of approximately 1-3 μm providing a larger active surface area and exposing more active sites[7], the TEM images further confirm that CNFPO possesses an ultrathin nanosheet structure (Supplementary Figure S2b). The addition of sodium hypophosphite altered the crystalline structure of the trimetallic alloy. Selected-area electron diffraction (SAED) patterns and high-resolution transmission electron microscopy (HRTEM) images reconfirmed the amorphous nature of CNFPO, showing no lattice fringes (Supplementary Figure S2c). In contrast, the CNFO sample exhibits clear lattice fringes (Figure R22g), with interplanar spacings of approximately 0.230 nm, 0.233 nm, and 0.245 nm, corresponding to the (015) plane of CoFe LDH, the (015) plane of NiFe LDH, and the (023) plane of Fe_2O_3, respectively.

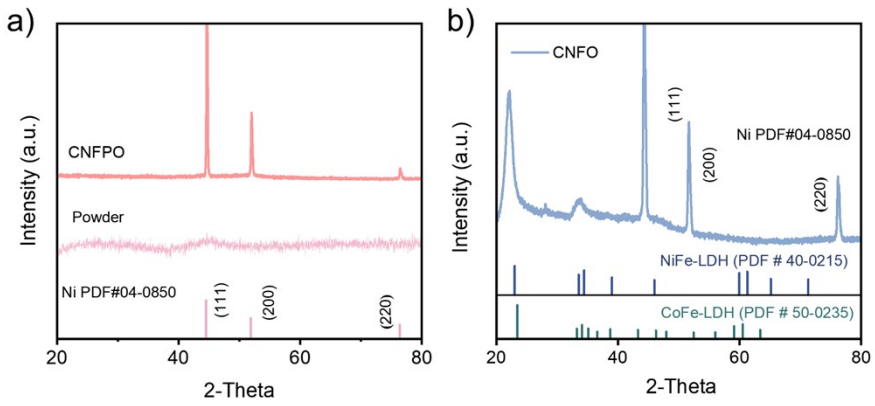

Figure S5. XRD analysis of pre-catalysts. XRD patterns of CNFPO (a) and CNFO (b). The XRD pattern of CNFPO Supplementary Figure S3a shows that the prepared electrode has an amorphous structure. Except for the diffraction peaks corresponding to the (111), (200), and (220) planes of the nickel foam substrate (PDF#04-0850), no additional diffraction peaks are observed, confirming the amorphous nature of the CNFPO electrode. In contrast, the XRD spectra of CNFO (Supplementary Figure S3b) show an ordered crystal structure.

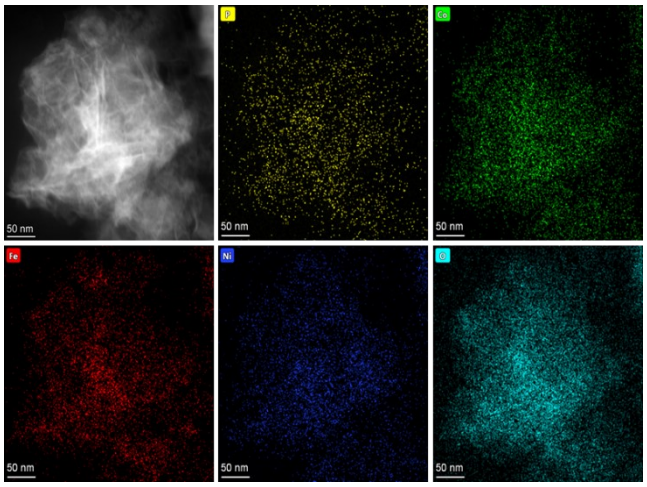

Figure S6. HRTEM image and the corresponding EDS mapping of CNFPO.

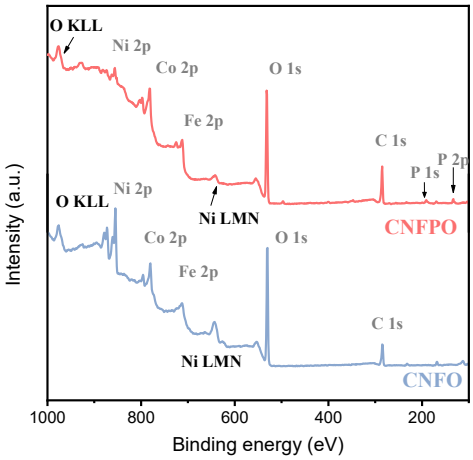

Figure S7. XPS total spectrum of CNFPO and CNFO. XPS spectra were employed to analyze the surface composition and valence states of CNFPO and its comparative samples. As shown in Supplementary FigureS5, the coexistence of Ni, Co, Fe, O, and P elements was observed, which is consistent with the EDS results.

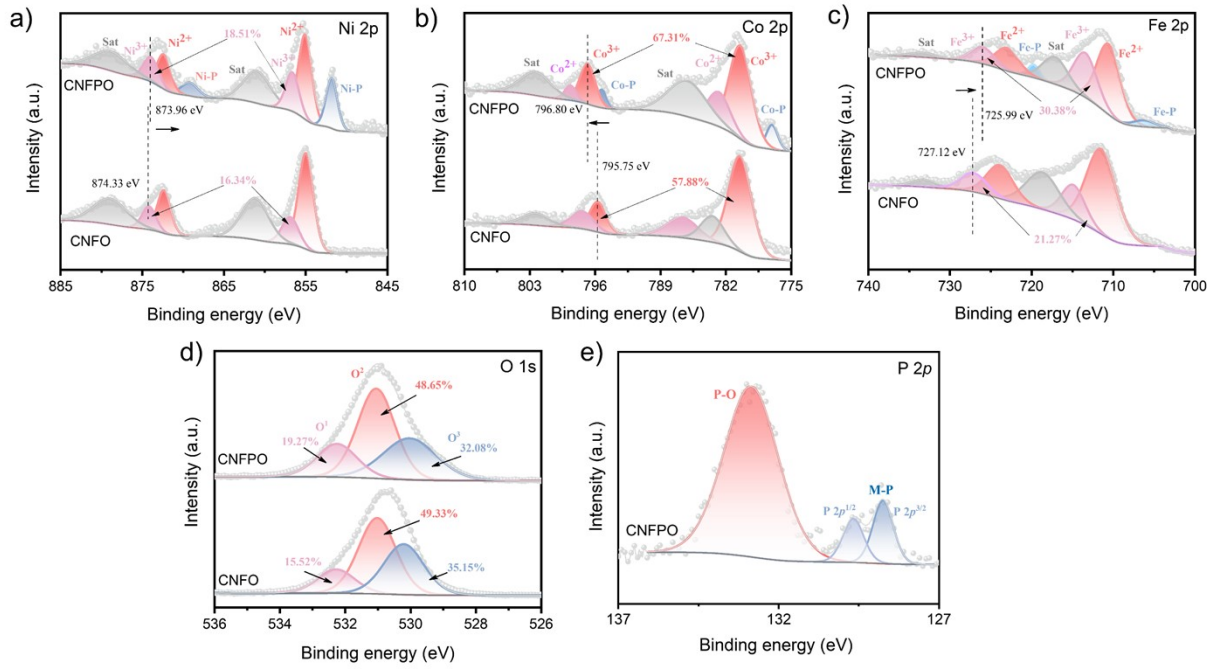

Figure S8. XPS spectra of CNFPO and CNFO. XPS spectra of Co 2p (a), Ni 2p (b), Fe 2p (c), O 1s (d), P 2p (e) of as-prepared CNFPO and CNPO. High-resolution Co 2p, Ni 2p, and Fe 2p spectra reveal peaks corresponding to Co-P, Ni-P, and Fe-P bonds, confirming M-P formation before reaction. Peak shifts indicate electron transfer and redistribution induced by electronegative phosphorus[8]. An increased ratio of trivalent to divalent metals suggests phosphorus optimizes the electronic structure, promoting high-valence Co, Ni, and Fe formation. The O 1s spectrum of CNFPO (Supplementary Figure S5e) exhibits three peaks, labeled O^1, O^2, and O^3. with contributions from M-O (530.05 eV), P-O (531.02 eV), and OH (532.00 eV). The M-O and OH peaks in CNFPO are primarily provided by hydroxides[9]. The increased proportion of the O^1 peak suggests that phosphorus incorporation enhances water adsorption on the catalyst surface, consistent with subsequent heavy water Raman and molecular dynamics simulation results. In the P 2p spectrum (Supplementary Figure S5f), peaks at 128.28 and 129.15 eV are assigned to M-P bonds, further confirming the formation of phosphides. The peak at 133.01 eV corresponds to P-O bonds in phosphates, which play a critical role in chloride suppression during seawater electrolysis.

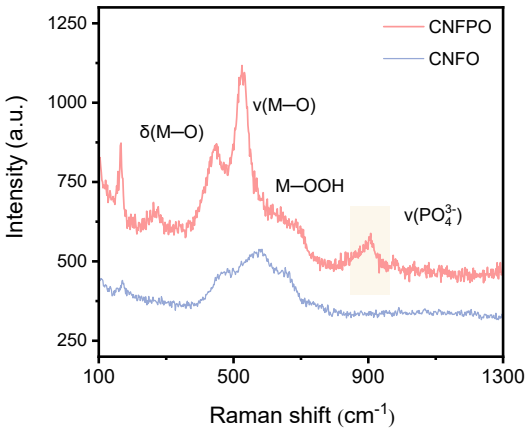

Figure S9. Raman spectra. In the Raman spectra,in the 400–700 cm^{-1} region shows broad M–O/M–OH (M = Co, Ni, Fe) vibrational characteristic bands, consistent with typical multi-metal oxide (hydroxide) features; a distinct P–O stretching vibration peak in the 900–1000 cm^{-1} region corresponds to the presence of phosphate (PO3- 4).

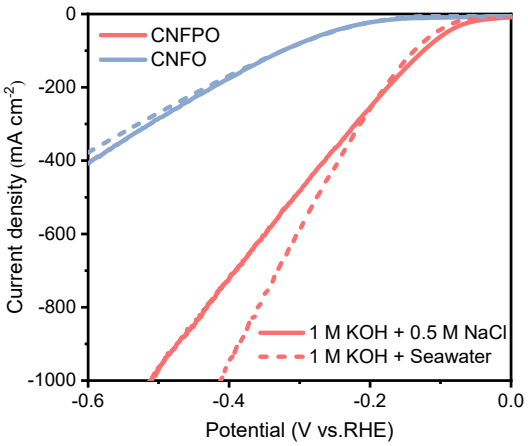

Figure S10. HER polarization curves for CNFPO and CNFO in 1 M KOH simulated seawater and 1 M KOH real seawater electrolytes (with 75% IR compensation). The CNFPO catalysts still maintained outstanding catalytic activity for HER in alkaline simulated seawater (1.0 M KOH + 0.5 M NaCl) /natural seawater (1.0 M KOH + real seawater, pH = 7.84 ± 0.02; Qingdao, China) electrolytes, as shown in Supplementary Figure S8, HER in alkaline simulated seawater required overpotentials of 22 and 132 mV, respectively, that could potentially reach a current density of 10/100 mA cm^{-2}, and HER in alkaline natural seawater required overpotentials of 24 and 148 mV, respectively, that could potentially reach a current density of 10/ 100 mA cm^{-2} current density. This is very close to the current density observed in a 1.0 M KOH electrolyte environment.

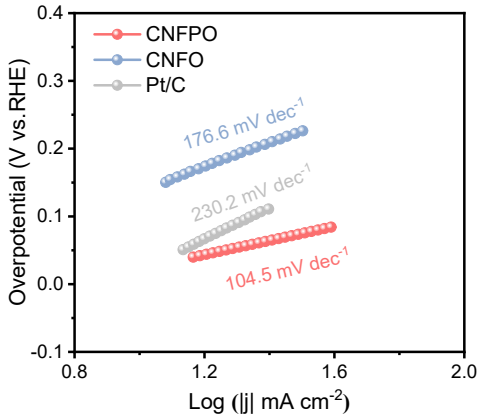

Figure S11. Tafel plots. The reaction kinetics of the different samples were studied using Tafel slopes converted from the corresponding LSV curves. Typically, smaller Tafel slopes correspond to faster reaction kinetics. As shown in Supplementary Figure S9, the Tafel slope of CNFPO was only 104.5 mV dec^{-1}, far smaller than that of the CNFO and Pt/C. The advantages of CNFPO sample in HER kinetics were highlighted.

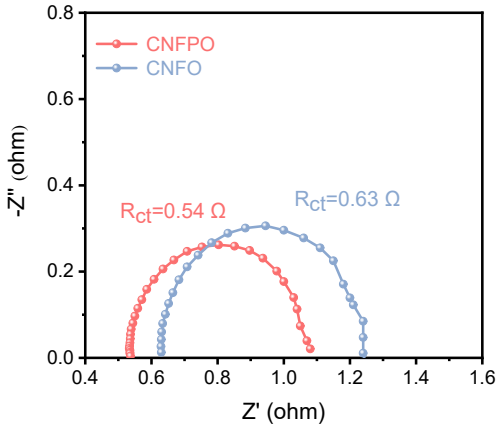

Figure S12. EIS Nyquist plots of HER-activated electrodes. EIS plots are operated to measure the charge transfer resistance of HER-activated electrodes. The charge-transfer resistance (Rct) of CNFPO (0.54 Ω) is smaller than that of CNFO (0.63 Ω), implying the more rapid electron transfer capacity among the interior and contact surface between electrode and electrolyte.

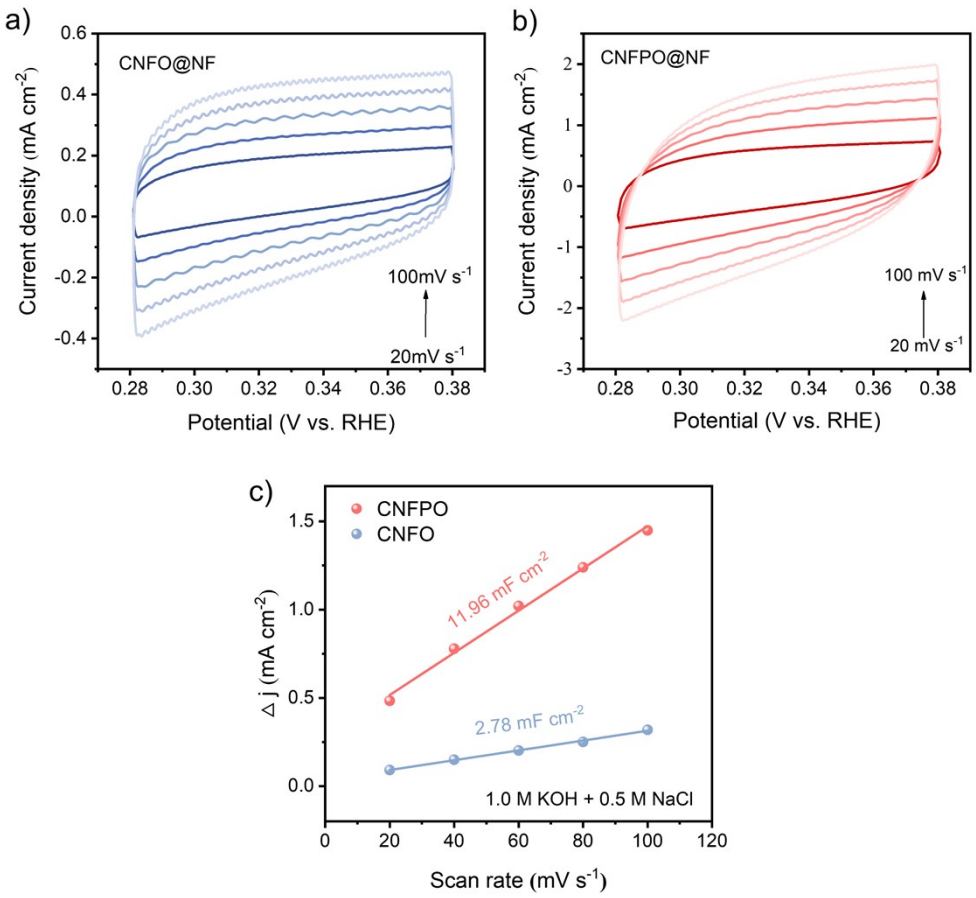

Figure S13. CV curves with different scan rates and the capacitive current-scan rate plots.CV curves with different scan rates. (a) CNFPO, (b) CNFO. (c) C_{dl} comparisons by dividing the double layer charging current differences with the scan rates. Cyclic voltammetry was used to determine the capacitance of the material's double layer (C_{dl}) by testing in the non-Faraday region at different scan rates. The C_{dl} of CNFPO was 11.78 mF cm^{-2}, which is approximately four times that of the control, suggesting that the CNFPO catalyst has a larger active surface area.

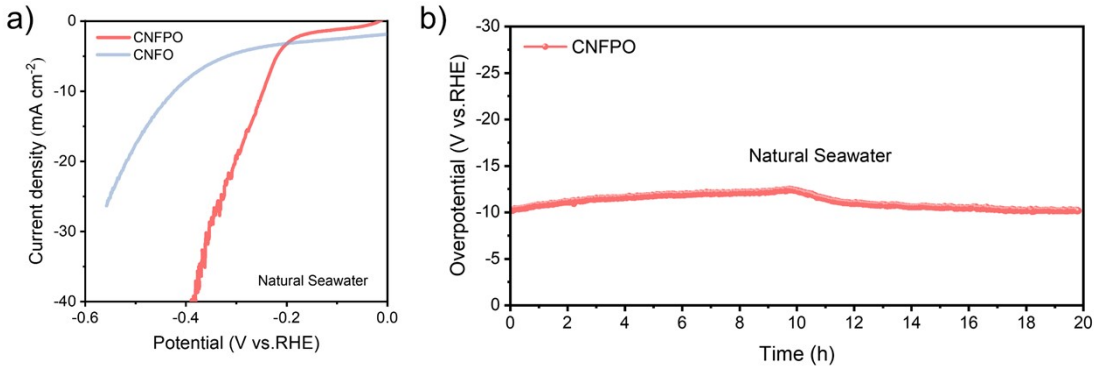

Figure S14. a) LSV curves of CNFPO and CNFO in natural seawater. b) Stability of CNFPO in natural seawater at 10 mA cm^{-2}. The results demonstrate that the catalyst still performs well in direct seawater electrolysis, requiring only a 243 mV overpotential to drive a current density of 10 mA cm^{-2}. Additionally, the current density shows almost no decay after 20 hours of testing. This performance is comparable to that of recently reported natural seawater HER catalysts (Table S3), further confirming the catalyst's potential in direct seawater electrolysis.

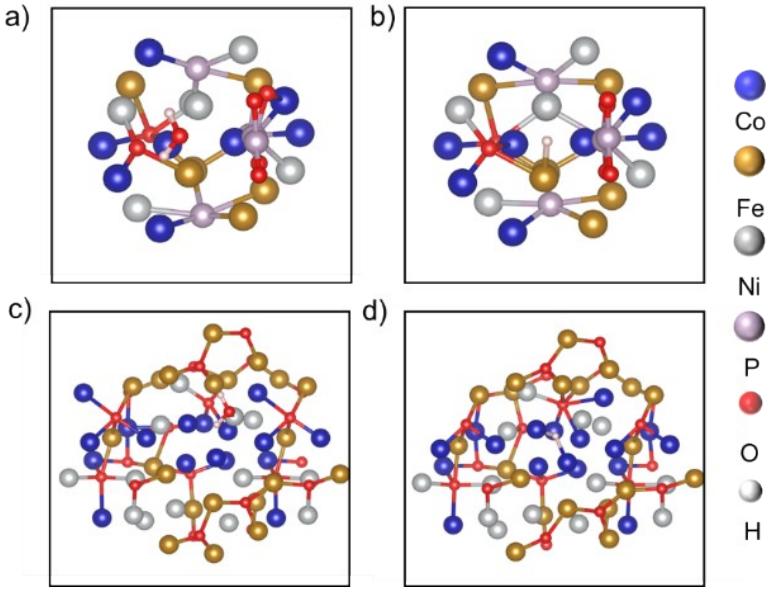

Figure S15. The DFT calculated structural models. Chemisorption models of (a) H_2O and (b) H on the CNFPO. Chemisorption models of (c) H_2O and (d) H on the CNFO. we employed a cluster-based approach to model the local coordination environment, which is a well-established practice for amorphous or poorly crystalline materials where long-range order is absent but short-range order persists. Co is represented in blue, Ni in silver, Fe in brown, P in purple, O in red, and H in white.

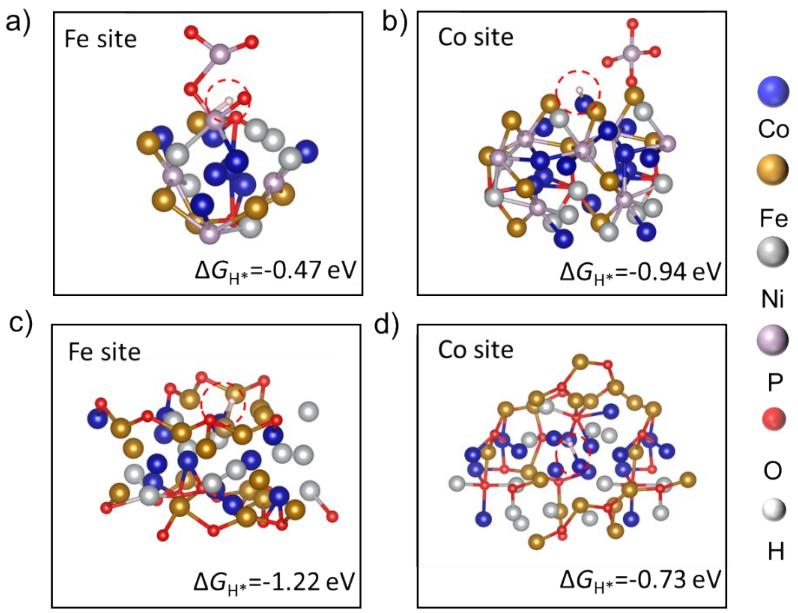

Figure S16. H* adsorption models and corresponding adsorption energies on Co and Fe sites of CNFPO and CNFO. our calculations reveal that while both Co and Fe sites were considered in each model, the introduction of phosphate doping in CNFPO fundamentally alters the relative adsorption energetics. In the phosphate-doped CNFPO system, the Fe site exhibits the most thermodynamically favorable hydrogen adsorption free energy (ΔGH*) among all evaluated positions, whereas in the phosphate-free CNFO system, the Co site proves to be the optimal adsorption center.

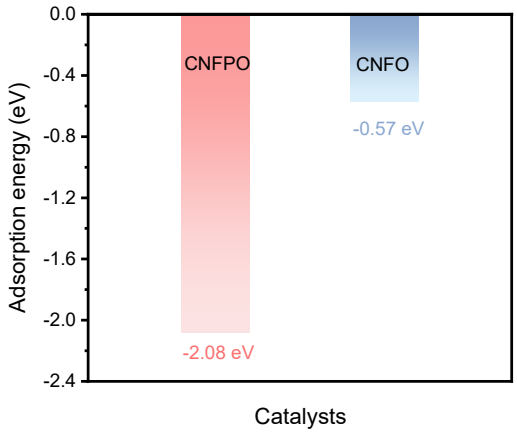

Figure S17. Water adsorption energy of CNFPO and CNFO. The water adsorption energy was calculated for two different catalysts. The results demonstrate that the CNFPO catalyst exhibits significantly higher water adsorption capacity, indicating its superior hydrophilicity compared to the CNFO catalyst. This enhanced hydrophilic property facilitates the subsequent water enrichment phenomenon on the catalyst surface as discussed in later sections.

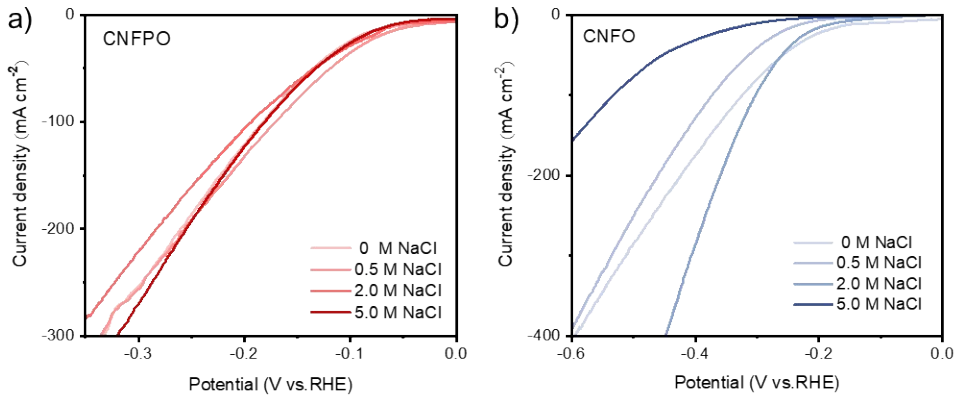

Figure S18. Salt-resistant electrocatalytic properties (with 75% IR compensation). (a–b) LSV curves of CNFO and CNFPO for the HER in different salt solutions. Electrochemical tests showed (Supplementary Figure S15) that the overpotential of CNFPO increased only about 5 mV when the NaCl concentration was elevated from 0 M to 5.0 M, underscoring its exceptional salinity tolerance. In stark contrast, the undoped CNFO catalyst suffered significant performance decay under the same conditions, highlighting the detrimental effect of Cl− on conventional catalytic.

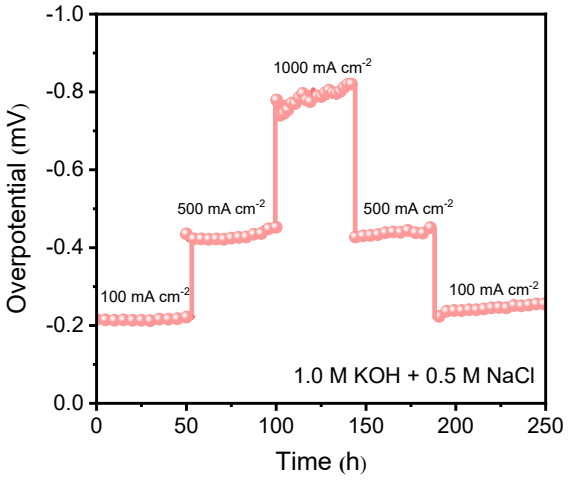

Figure S19. Multi-step chronopotentiometry curve. The chronoamperometry curve of CNFPO for a continuous 250 h operation at different current densities of 100, 500, and 1000 mA cm^{-2}. Long-term durability was confirmed by a 1200 h chronoamperometry test at 50 mA cm^{-2} (Figure 2b) and stepwise current testing at 100, 500, and 1000 mA cm^{-2} over 250 h (Supplementary Figure S16). The CNFPO catalyst demonstrated remarkable operational stability, unequivocally validating CNFPO's exceptional resistance to chlorine corrosion.

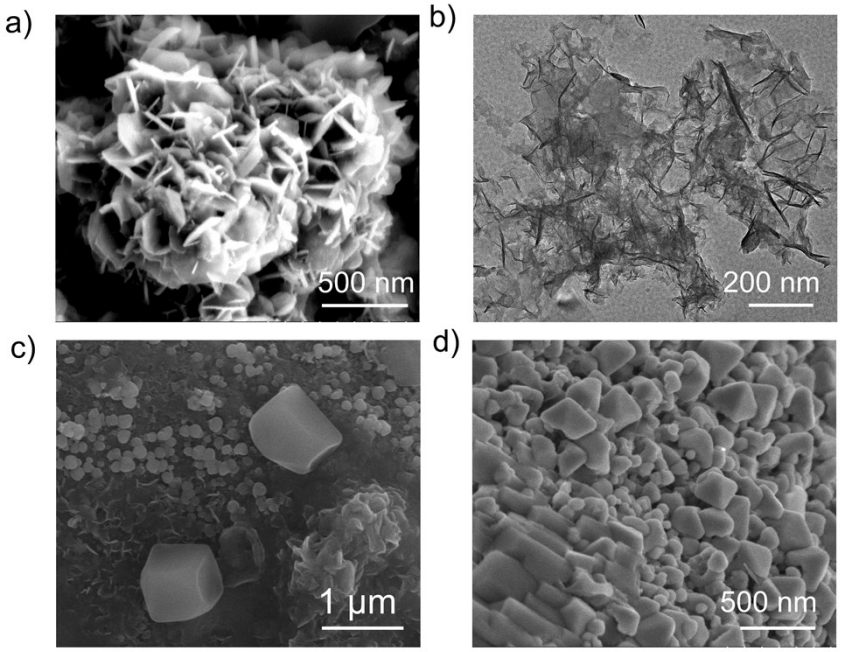

Figure S20. Structural characterization after reaction. SEM images and TEM images after stability testing of CNFPO (a, b) and CNFO (c, d). The CNFPO nanosheets still maintain their original morphology with only a small amount of NaCl particles attached during long-time operation. And the accumulation of a large number of NaCl particles on the CNFO nanosheets further proves its good salt resistance.

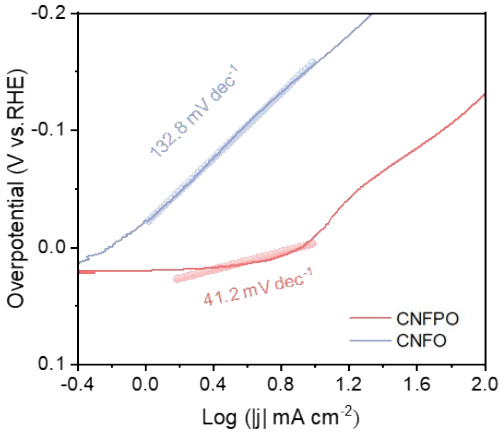

Figure S21. Tafel plots of CNFPO and CNFO. These free water molecules exhibit higher orientational freedom and proton transfer activity, making them key reactants for the Volmer step ($H_2O + e^- \rightarrow H_{ads} + OH^-$) in the IHP region. CNFPO exhibits an ultra-low Tafel slope of 41 mV dec^{-1}, a value consistent with the Volmer–Heyrovsky mechanism in the low current region (1–10 mA cm^{-2}), where the electrochemical hydrogen adsorption/desorption (Heyrovsky step: $H_2O + M–Hads + e^- \rightarrow M + H_2\uparrow + OH^-$) is the rate-determining step (RDS). In stark contrast, CNFO exhibits a Tafel slope of 112 mV dec^{-1}, which is characteristic of process limited by the Volmer step. This mechanistic shift strongly suggests that the enriched population of free water at the CNFPO interface provides a continuous supply of dissociable H_2O molecules, thereby accelerating proton transfer and lowering the kinetic energy for water dissociation.

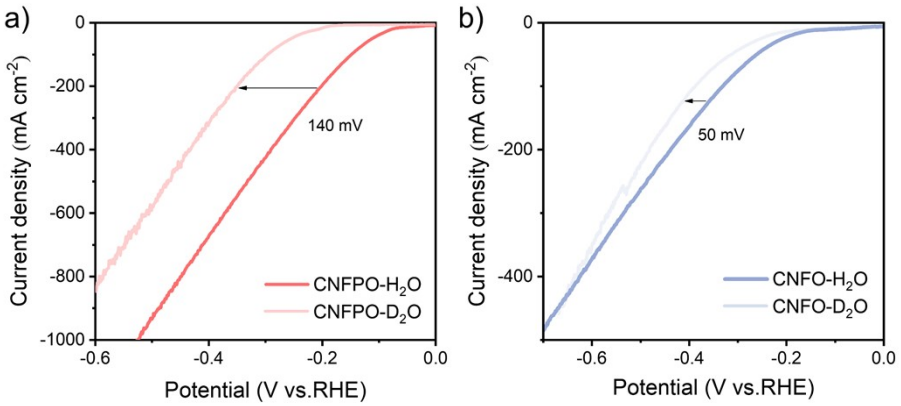

Figure S22. H_2O/D_2O isotope substitution experiment of CNFPO (a) and CNFO (b). The presence of free water in the IHP was further verified through H_2O/D_2O isotope substitution experiments. The results reveal that CNFPO exhibiting a pronounced KIE, with its HER activity substantially attenuated in the D_2O-based electrolyte. Conversely, the isotope effect for CNFO is markedly weaker. This indicates that H_2O molecules in the CNFPO interface are free to participate in the Volmer step, while water in CNFO exists more in a bound state. This directly confirms our conclusion that " an accumulation of free water within the IHP and governs enhanced HER kinetics of CNFPO."

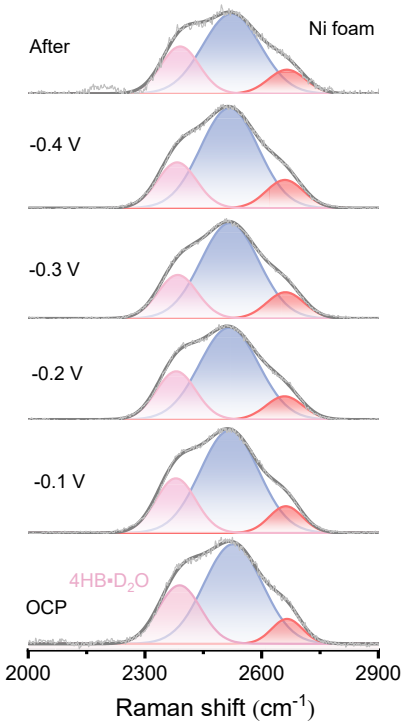

Figure S23.In situ Raman (using D2O) spectra of pure Ni foam. We conducted a critical control experiment using pristine Ni foam as a reference sample under identical operando conditions. In contrast to the CNFPO electrode, the O-D stretching vibration bands on the bare Ni foam surface exhibited no such evolution or spurious peaks throughout the applied potential range.

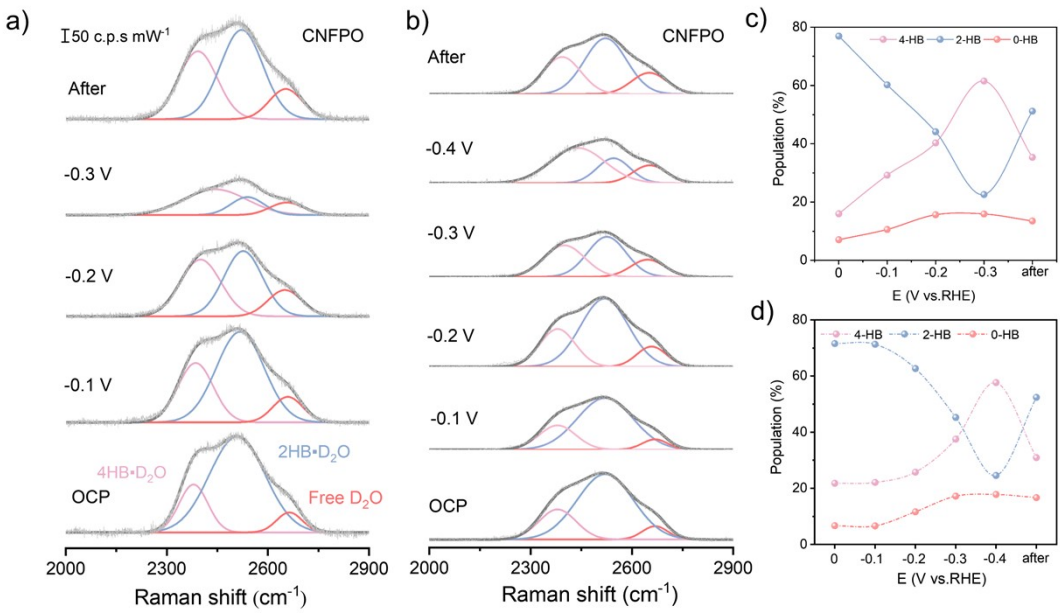

Figure S24.Reproducibility Raman tests of two independently prepared CNFPO samples. To rigorously validate the reproducibility of this key finding, we performed repeated *in situ* deuterated water Raman experiments on two independently prepared CNFPO samples. The results were highly consistent: all samples exhibited the same spectral evolution trend under polarization, with the proportion of 4HB·D_2O increasing from an initial range of 15–25% to a final range of 58–68%. This consistent observation across multiple samples provides robust statistical validation for our results and effectively rules out the possibility that this is an anomalous result or a fitting artifact.

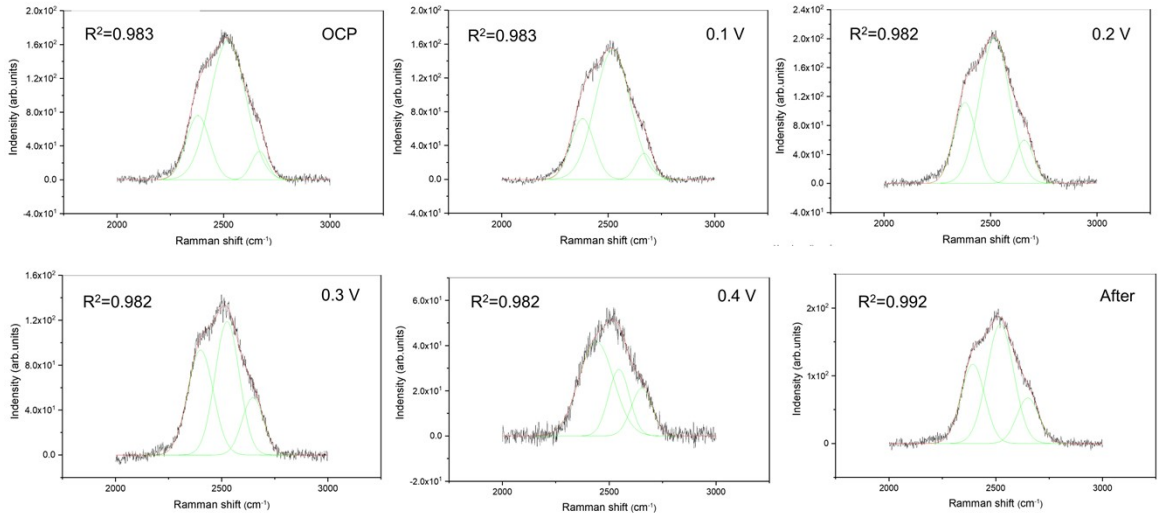

Figure S25. Original Raman spectra and corresponding peak fitting diagrams. Following standard practice, peak deconvolution was performed using a Gaussian model. The full widths at half maximum (FWHM) were constrained within physically reasonable bounds for each dataset, and fits were optimized by minimizing residuals. The fitting quality was consistently high, with R^2 values exceeding 0.98 for all deconvoluted curves (Figure R3). Collectively, these controls substantiate the reliability of our deconvolution approach and the derived population trends.

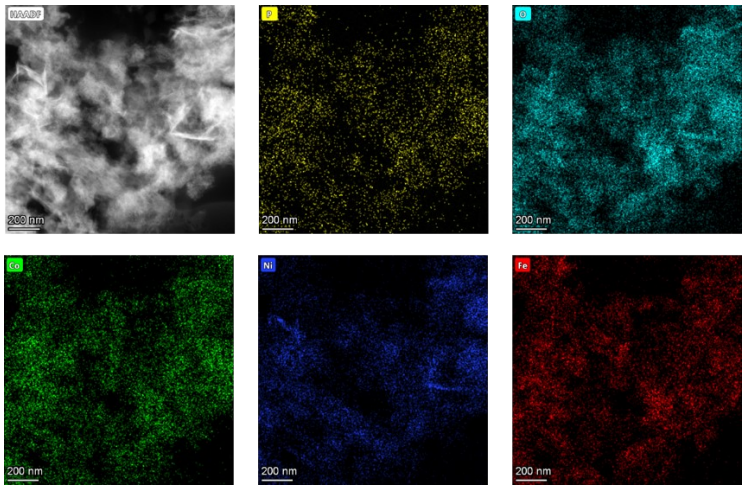

Figure S26. HRTEM-EDS elemental mapping of reacted CNFPOs. The EDX elemental mapping after the reaction still shows a uniform distribution of the three metals. In addition, after HER, the distribution of P element was significantly weakened from 3.06% to 0.90% and was mainly distributed on the surface of the catalyst, and we speculate that P was first leached from the matrix and then oxidized and adsorbed as a phosphate on the surface of CNFPO.

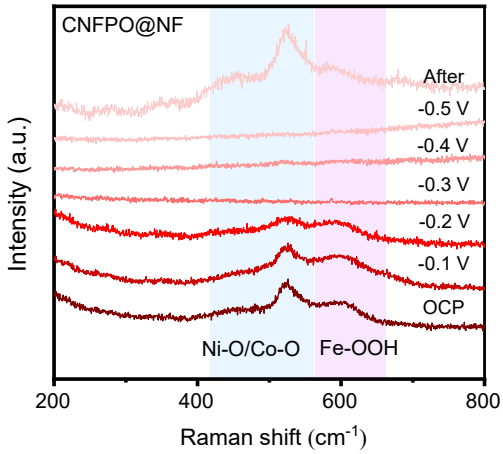

Figure S27. In situ Raman spectra of CNFPO. In the in situ Raman spectra, as shown Supplementary Figure S18, it can be observed that the Raman vibrational intensities of the Fe-OOH and Ni-O/Co-O bonds significantly decrease and further disappear at -0.2 V, Crucially, these bands reappeared after the end of the reaction, confirming that low-valent metal species serve as the HER-active phases during cathodic operation while spontaneously reoxidizing to stable high-valent hydroxyl oxides upon reaction cessation[11].

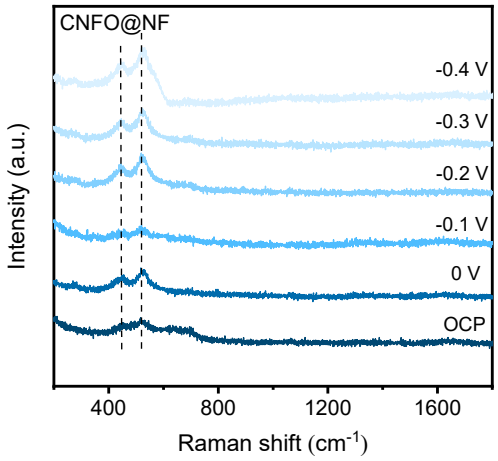

Figure S28. In situ Raman spectra of CNFO. In situ Raman spectra of CNFO, the Raman vibration of Fe-OOH bond further decreases while the intensity of the Raman vibration of Ni-O/Co-O bond enhances with the increase of negative potential. We suggest that during HER, the CNFO catalyst accelerates HER by promoting the formation of $Ni(OH)_2$, $Co(OH)_2$ at high cathodic potentials.

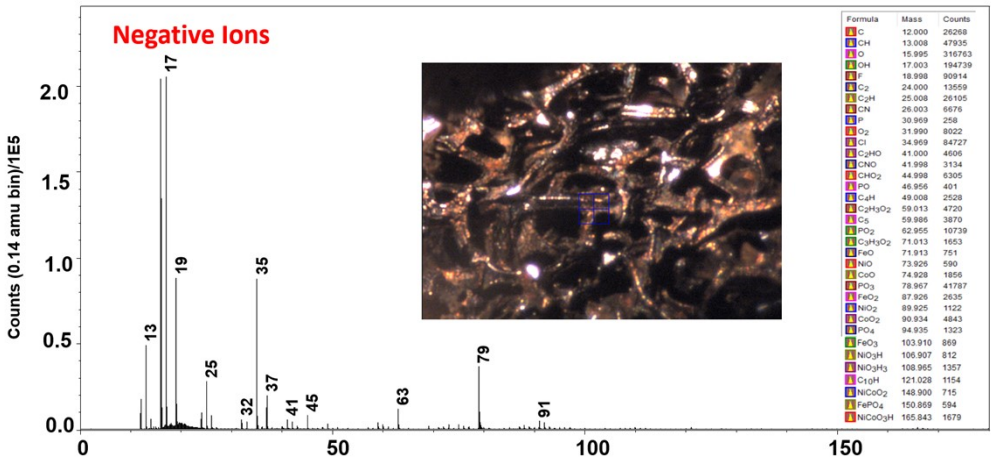

Figure S29. Time-of-flight secondary ion mass spectrometry (TOF-SIMS) analysis. Secondary ion mass spectrometry TOF-SIMS detected the anionic and cationic groups on the surface of the catalyst after the reaction, and among the anionic groups, phosphorus-containing signals were found at m/z = 47, 63, 79, and 95, corresponding to PO, PO_2, PO_3, and PO_4,[11] indicating the presence of phosphate adsorption during the reaction. In addition, a large number of OH ionic groups, including Ni-OH, Fe-OH, and Co-OH, were detected, indicating that the catalyst surface was enriched with OH groups after the reaction .

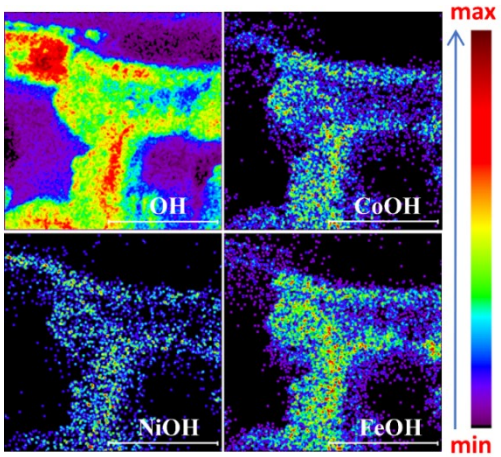

Figure S30. TOF-SIMS detection of enriched OH groups. A large number of Ohydrogen-ion groups were detected on the surface of the catalyst after HER reaction, including Ni-OH, Fe-OH, and Co-OH, suggesting that the surface of the reacted catalyst was enriched with Ohydrogen-groups, which was consistent with the inference that the M-P in the reacted XPS tended to be converted into the active sites M-O/M-OH. In alkaline seawater, the increase in sodium and chloride ions would impede the dissociation of water on the surface of the electrode and the transport of H_2O*/OH* intermediates, which would be greatly alleviated by Ohydrogen-groups, and the surface-enriched OH− groups facilitate the enhancement of HER activity[12].

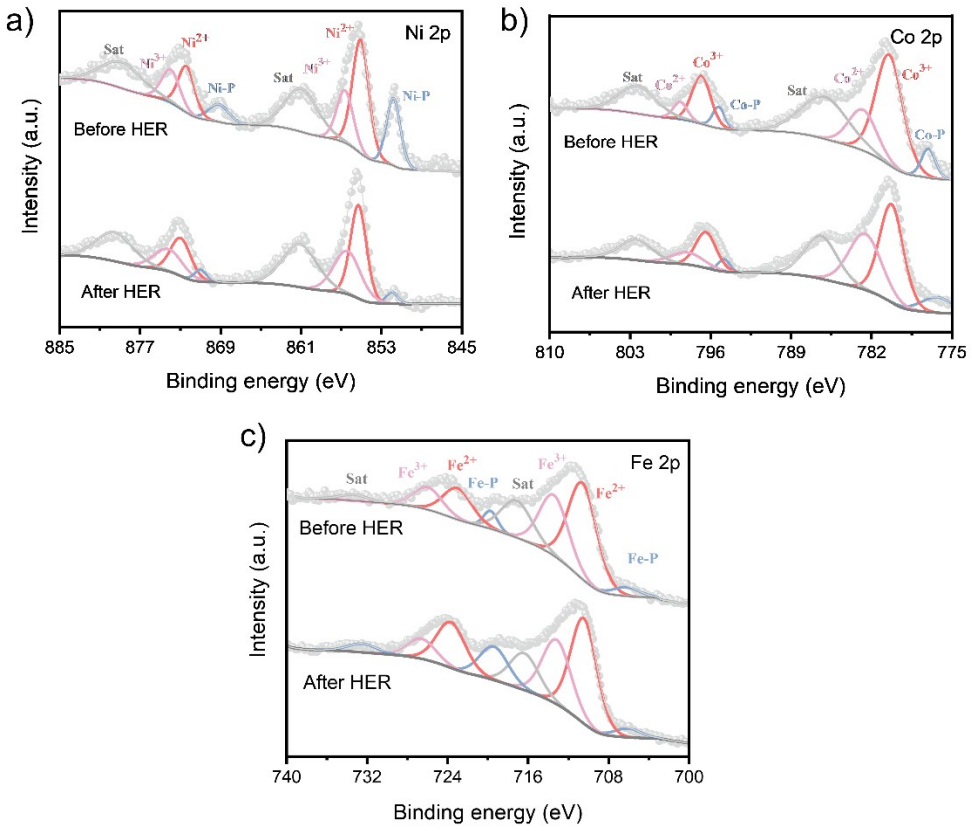

Figure S31. XPS spectra of CNFPO before and after 30 h HER stability test. High-resolution XPS spectra of (a) Ni 2p, (b)Co 2p, and(c) Fe 2p, for CNFPO before and after 30 h HER stability test. Cathodic XPS measurements after 30-h of testing showed that all M-P peak intensities were reduced and all shifted slightly towards lower binding energies. This indicates that during the prolonged HER stability test, more metal hydroxide/(oxy)hydroxide release of M-P converted to the active sites M-O/M-OH, with phosphorus predominantly in the form of phosphates and phosphates.

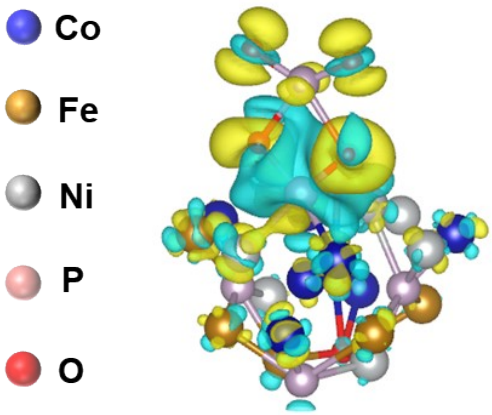

Figure S32. Differential charge density of PO_4^{3-} adsorbed by CNFPO

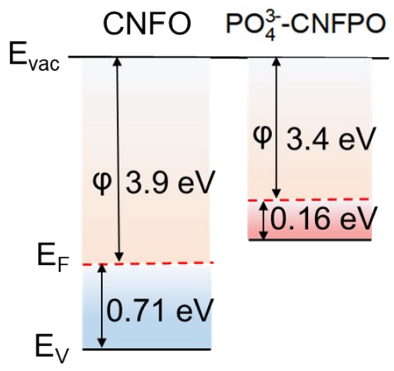

Figure S33. Comparison of power function values for PO3- 4-CNFPO and CNFO. To further characterize interfacial charge variations, ultraviolet photoelectron spectroscopy (UPS) was employed to investigate PO3- 4-CNFPO and CNFO. The cutoff energy (E_{cutoff}) and valence band (E_v) binding energy values for both samples were determined through linear extrapolation of UPS spectra and XPS valence band spectra. The work function (W_F) was calculated using the following equation: $W_F = hv - |E_{cutoff} - E_{feimi}|$.where hv (He I excitation energy) is 21.22 eV and E_{feimi} is 0 eV. The work functions of CNFPO and CNFO were measured to be 3.9 eV and 3.4 eV, respectively[13].

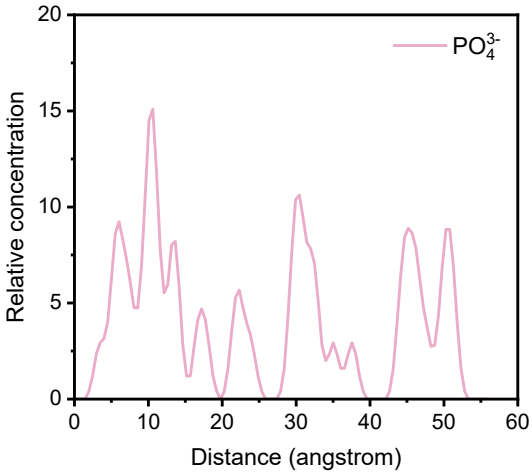

Figure S34. Molar concentration of PO3− 4 as a function of distance above the electrode surface. The statistics of the molecular dynamics simulation results in the aggregation of phosphate groups on the surface of the CNFPO catalyst, with a peak concentration within 5Å.

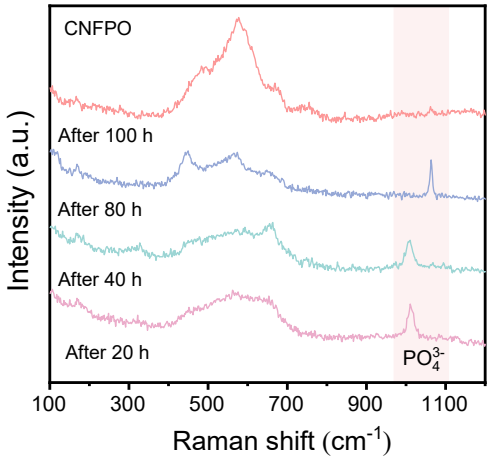

Figure S35. Raman spectra at different time points after the HER reaction. The results show that the 1000–1100 cm^{-1} (PO3- 4) characteristic peak in CNFPO remains stable after long-duration reactions, proving that the interfacial phosphate structure has good durability, supporting our conclusion that PO3- 4 stably regulates the interfacial water structure. We observed a blue shift in the phosphate vibrational peak as the reaction time increased. We believe this phenomenon indicates a stronger interaction between the PO3- 4 and the catalyst surface during the reaction. Specifically, the adsorption strength between the PO3- 4 and the catalyst surface increases, possibly due to changes in the surface charge density, which results in a more tightly bound vibrational mode of the phosphate ions.

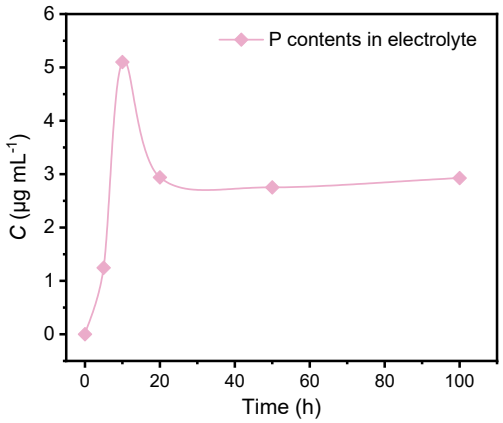

Figure S36 ICP-MS. the quantitative detection of phosphate content in the electrolyte was performed via ICP-MS. A small amount of phosphate (P) was detected at the onset of the reaction, signifying an initial leaching from the CNFPO bulk. The concentration peaked at approximately 5 hours and subsequently decreased after 10 hours during the HER measurement, indicating that phosphate ions establish in a dynamic equilibrium between surface adsorption and migration. Over extended operation, the phosphate concentration stabilized, confirming that a steady state between dissolution and re-adsorption is maintained. After 100 hours of continuous HER, the total amount of leached phosphate was only a small fraction of the total phosphate content, with no significant loss.

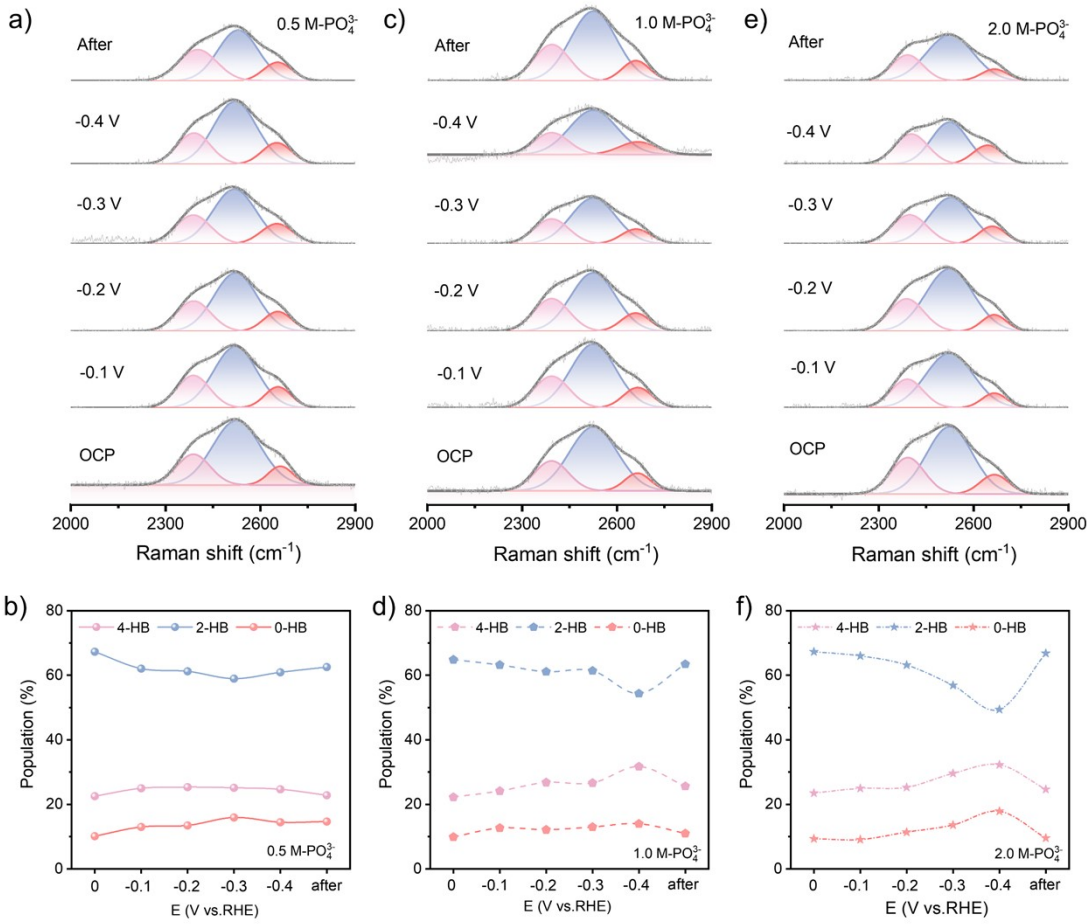

Figure S37 In-situ Raman spectra and corresponding interfacial water configuration ratios with different concentrations of potassium phosphate in the electrolyte: 0.5 M (a, b), 1.0 M (c, d), and 2.0 M (e, f). The results show that adding phosphate ions does not significantly alter the O–D vibrational structure of water, inducing only a minor peak shift. This effect is substantially weaker than the profound evolution of interfacial water induced by dynamic migration in the CNFPO system.

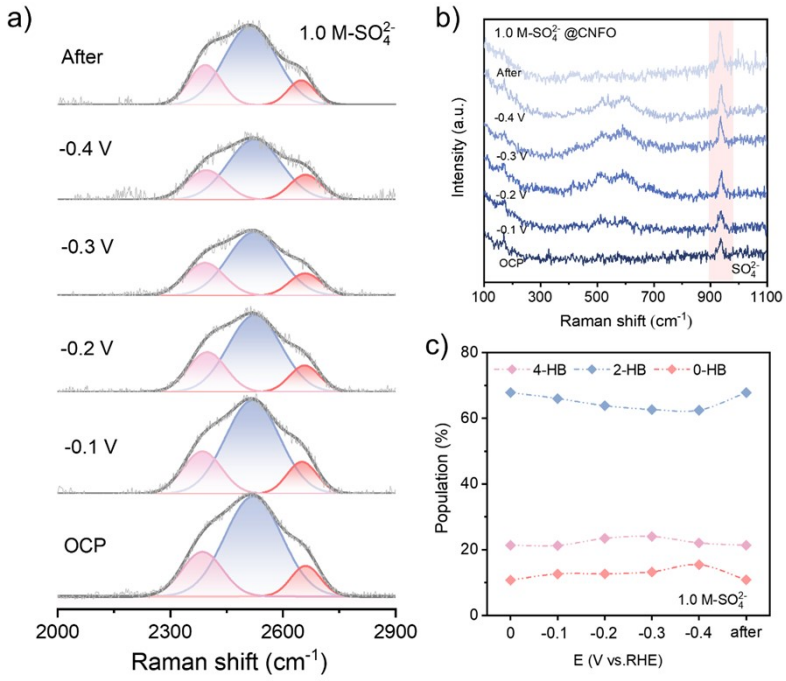

Figure S38 a) In-situ D_2O Raman spectra of the electrolyte with 1.0 M potassium sulfate, b) In-situ Raman spectra, and c) Interfacial water molecule population ratios. In Figure S33, the peak at 950 cm^{-1} corresponds to the vibrational mode of sulfate ions (SO2- 4). Upon addition of sulfate to the electrolyte, we detect a progressive increase in this peak's intensity during reaction, indicative of SO2- 4 accumulation at the catalyst–electrolyte interface. This behavior is consistent with electrochemical adsorption of SO2- 4 onto the catalyst surface. We examined other anion systems (SO2- 4) and found that their effects on hydrogen bond structure were also limited. This finding unequivocally demonstrates that the formation and sustenance of the ice-like water film is not a simple surface adsorption phenomenon. Instead, it is a direct consequence of the synergistic interplay between catalyst surface reconstruction and the electrofield-driven migration of in situ generated phosphate species. It is this unique dynamic that establishes the robust, 4-coordinate hydrogen-bond network required to effectively repel chloride ions.

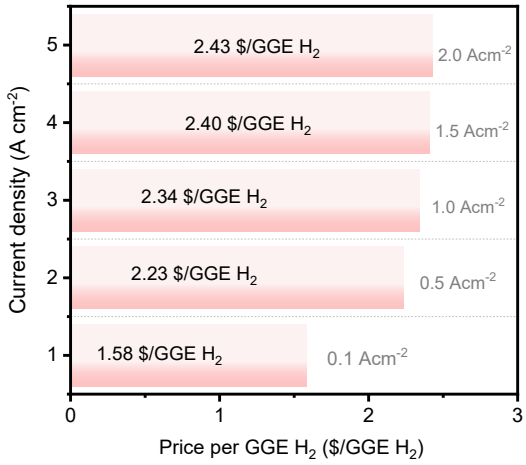

Figure S39. Price per GGE H_2 of CNFPO || CoFe-LDH.

H_2 production rate@0.1 A cm^{-2}

$$= (j\ A\ cm^{-2}) \times (1\ e^{-}/1.602 \times 10^{-19} C) \times (1\ H_2/2\ e^{-})$$

$$= 0.1\ A\ cm^{-2}/(1.602 \times 10^{-19}\ C \times 2) = 5.18 \times 10^{-7}\ mol\ H_2\ cm^{-2}\ s^{-1}$$

LHV of H_2

$$= 120\ kJ\ g^{-1}\ H_2 = 2.42 \times 10^{5}\ J\ mol^{-1}\ H_2$$

H_2 power out

$$= (5.1828 \times 10^{-7}\ mol\ cm^{-2}\ s^{-1}) \times (2.40 \times 10^{5}\ J\ mol^{-1}) = 0.1243\ W\ cm^{-2}$$

Electrolyzer Power @ 0.1 A cm^{-2}

$$= (0.1\ A\ cm^{-2}) \times (1.372\ V) = 0.1372\ W\ cm^{-2}$$

Efficiency of AEM

$$= (H_2\ Power\ Out)\ /\ (Electrolyzer\ Power) = 0.1243\ W\ cm^{-2}/0.1372\ W\ cm^{-2} = 90.6\%$$

Energy consumption

$= 9.6485 \times 10^7 \times 1.372/3.6 \times 10^6 = 36.76\ kWh/kg\ H_2$

we examined the cost components of hydrogen production in actual operations, using the cost estimate for a 1 MW alkaline seawater electrolyzer as an example. We considered factors such as AWE stack components and prices, water price, electricity price, catalyst preparation costs, maintenance rates, labor rates, and plant lifetime. The actual electricity price was adjusted to $0.03/kWh, and the electricity cost proportion was recalculated as 0.83 * 0.83 = 68.89%.

Price per gasoline-gallon equivalent (GGE) H_2

$= 1\ GGE\ H_2/H_2\ production\ rate \times Electrolyzer\ power \times Electricity\ bill$

$= 0.997\ kg\ /\ (5.1828 \times 10^{-7}\ mol\ H_2.cm^{-2}\ s^{-1} \times 2\ kg/mol) \times 0.1372\ W\ cm^{-2} \times \$\ 0.03\ /\ kW\ h/68.89\%$

$= \$\ 1.58\ /GGE\ H_2$

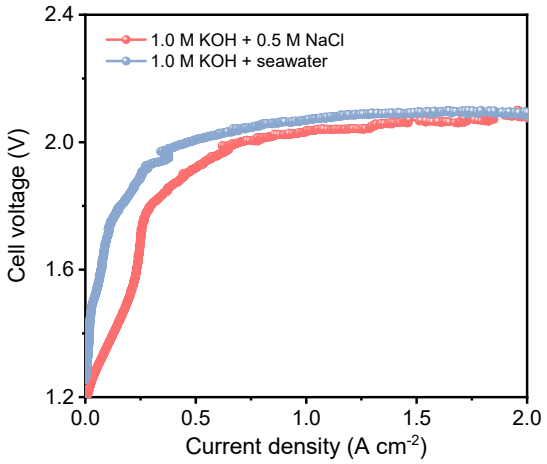

Figure S40. CNFPO || CoFe-LDH in the polarization curves of AEM electrolyzer operated in alkaline simulated seawater (1 M KOH + 0.5 M NaCl) and alkaline natural seawater (1 M KOH + seawater) (IR compensation 50%). The device in alkaline natural seawater achieved an industrially relevant current density of 2 A cm^{-2} at only 1.97 V cell voltage, similar to the results obtained under simulated alkaline seawater conditions.

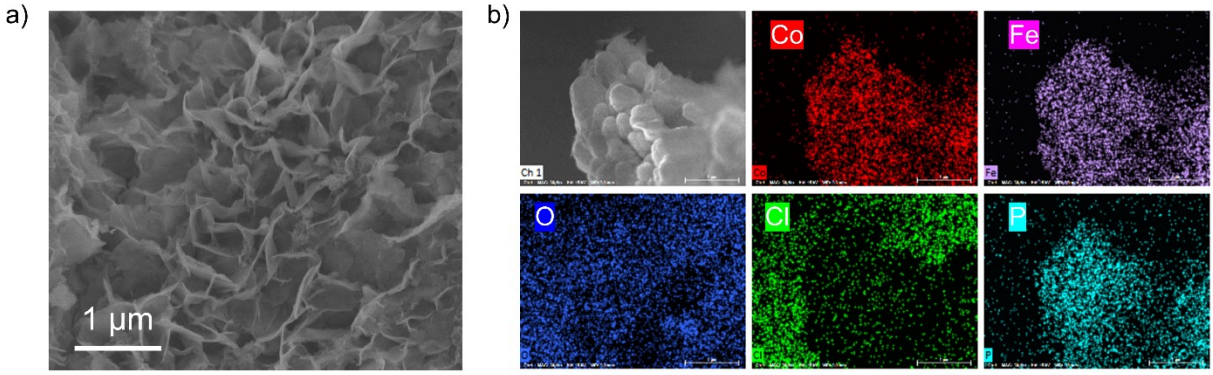

Figure S41. SEM image (a) and EDS mapping (b) of CNFPO after 1000 hours of membrane electrode device operation. even after 1000 hours of continuous membrane electrode operation, the nickel foam substrate maintains its good morphology, with only a small amount of chloride ions adhering and no significant corrosion observed.

Table S1. The elemental weight percentages in the catalyst CNFPO and CNFO determined by ICP-OES.

Catalyst	Co (wt.%)	Ni (wt.%)	Fe (wt.%)	P (wt.%)
CNFPO	3.716%	3.891%	3.916%	1.033%
CNFO	5.053%	6.735%	4.380%	0.000%

Table S2. Comparison of the HER activitie of CNFPO with recently reported electrocatalysts.

Catalyst	η_{10} in 1.0 M KOH (mV)	η_{10} in 1.0 M KOH + seawater (mV)	Time (h)	Reference
This work	11	24	1200	This work
CoPGT	103	114	60	*Nat. Commun.* **2023**, 14, 7708.
R-CoC_2O_4@MXene	--	32	100	*Nat. Commun.* **2022**, 13, 5785.
$NiMoO_4 \cdot xH_2O$	22	33	540	*Nat. Commun.* **2025**, 16, 3098
Pt_{SA}-$Ni_{6.6}Fe_{0.4}P_3$	20	134 (4 M NaCl)	120	*Nat. Commun.* **2023**, 14, 3934.
Ir/HfO_2@C	28	39	550	*J. Am. Chem. Soc.* **2024**, 146, 27486–27498.
GDY/MoO_3	170 (0.1M)	210	120	*J. Am. Chem. Soc.* **2021**, 146, 8720–8730.
Ru@NMoC	8	20	100	*Angew. Chem., Int.* Ed. **2025**, 64, e202505031.
Ru/$NiMoO_{4-x}$	--	42	750	*Angew. Chem., Int.* **2024**, 63, e202316319.
CoO-$Co_2Mo_3O_8$	20	31	300	*Angew. Chem., Int.* **2025**, 64, e202423863.
TiRu/Ti	--	105	10	*Angew. Chem., Int.* **2024**, 63, e202319798
Pt-Ni_3N@V_2O_3/NF	14	25	500	*Sci. Adv.* **2024**, 10, eadn1126.
RuMo/Cu_2O@C	18	24	800	*Adv. Mater.* **2025**, 37, e2416658
O_s-$Co(OH)_2$	--	25	100	*Adv. Mater.* **2025**, n/a, e2506512
RuMo/Cu_2O@C	18	24	800	*Adv. Mater.* **2025**, 37, e2416658
Fe-Ni_2P_v	--	26	100	*Adv. Mater.* **2024**, 36, 2307395
Mo_3Se_4-NiSe	26	84.4	50	*Adv. Mater.* **2023**, 36, 2305813
Ni-MoN	40	46	200	*Adv. Mater.* **2022**, 34, 2201774

Ni-SN/C	28	24	40	*Adv. Mater.* **2021**, 33, 2007508
Ru–BO_x–Ohydrogen-300	22	24	20	*Energy Environ. Sci.* **2024**, 17, 3888-3897
SA-$MoO_2/Ni_3(PO_4)_2$/NF	34	46	100	*Adv. Funct. Mater.* **2023**, 33, 2308191
Ru_3/OCNT	19	24	24	*Adv. Funct. Mater.* **2025**, n/a, 202503678
PtRu/WO_3-O_V	9	26	10	*Adv. Energy Mater*. **2024**, 14, 202402372

Table S3. Comparison of the HER activitie of CNFPO in natural seawater with recently reported electrocatalysts.

Catalyst	η_{10} in natural seawater (mV)	Reference
CNFPO	243	This work
Pt/WO_2	290	*J. Am. Chem. Soc.* 2024, 146, 50, 34711–34719.
Mo_2N	311	Nat. Commun., 2024, 37, 9462.
NCP/PC	280	Nat. Commun., 2024, 15, 2950.
B-Os	230	Angew. Chem. Int. Ed., 2025, 26, e202512710.

Table S4. Elemental contents before catalysis

Before HER	Element	Atomic Fraction (%)
CNFPO	Co	8.49
	Fe	7.38
	Ni	7.94
	P	3.06
	O	73.13

Table S5. Elemental contents after catalysis

After HER	Element	Atomic Fraction (%)
CNFPO	Co	6.38
	Fe	8.73
	Ni	3.45
	P	0.90
	O	80.54

Table S6. Calculations of AEM electrolyzer efficiency and H_2 cost at different current densities in 1.0 M KOH + seawater.

j (A cm^{-2})	Voltage (V)	Power consumption（kW•h/m^3）	Efficiency of AEM (%)	Price per GGE H_2 ($)
0.1	1.372	36.76	90.6	1.58
0.5	1.916	51.33	64.9	2.23
1	2.024	54.24	61.4	2.34
1.5	2.066	55.38	60.2	2.40
2	2.096	56.19	59.3	2.43

Table S7. Comparison of HER stability in alkaline seawater electrolysis.

Catalyst	Electrolyte	Current density ($A\ cm^{-2}$)	Time (h)	Reference
This work	1 M KOH + 0.5 M NaCl	0.5	1000	This work
CoPGT	1 M KOH+ saturated NaCl	0.01	60	*Nat. Commun*. **2023**, 14, 7708.
Y-NiMo/MoO_{2-x}	3 M KOH + seawater	1	24	*Nat. Commun*. **2025**, 16, 773.
Pt/Ni-Mo	1 M KOH + 0.5 M NaCl	0.5	24	*Adv. Funct. Mater.* **2021**, 31, 2010367.
NiCoPv@NF	1 M KOH + seawater	0.5	110	*Adv. Energy Mater*. **2024**, 14, 2400975.

References

1 G. Kresse and J. Furthmüller, *Comput. Mater. Sci*, 1996, **6**, 15–50.

2 G. Kresse and D. Joubert, *Phys. Rev. B*, 1999, **59**, 1758–1775.

3 J. P. Perdew, K. Burke and M. Ernzerhof, *Phys. Rev. Lett.*, 1996, **77**, 3865–3868.

4 S. Grimme, J. Antony, S. Ehrlich and H. Krieg, *J. Chem. Phys.*, 2010, **132**, 154104.

5 D. J. Chadi, *Phys. Rev. B*, 1977, **16**, 1746–1747.

6 A. K. Rappe, C. J. Casewit, K. S. Colwell, W. A. I. Goddard and W. M. Skiff, *J. Am. Chem. Soc.*, 1992, **114**, 10024–10035.

7 B. Deng, Z.-Y. Wu, E. Feng, L. Ma, Z. Wang, J. Chen, L. Eddy, A. Lathem, T. Wang, W. Chen, Y. Cheng, S. Xu, Q. Liu, B. I. Yakobson, H. Wang, Y. Zhao and J. M. Tour, *J. Am. Chem. Soc.*, 2025, **147**, 16129–16140.

8 L. Cao, Q. Luo, W. Liu, Y. Lin, X. Liu, Y. Cao, W. Zhang, Y. Wu, J. Yang, T. Yao and S. Wei, *Nat. Catal.*, 2019, **2**, 134–141.

9 Q. Fu, L. W. Wong, F. Zheng, X. Zheng, C. S. Tsang, K. H. Lai, W. Shen, T. H. Ly, Q. Deng and J. Zhao, *Nat. Commun.*, 2023, **14**, 6462.

10 J. Zhu, J. Chi, T. Cui, L. Guo, S. Wu, B. Li, J. Lai and L. Wang, *Appl. Catal., B*, 2023, **328**, 122487.

11 Q. Yu, Y. Fu, Z. Liu, X. Liu, L. Guo, T. Wang, J. Chi, Z. Wu and L. Wang, *Appl. Catal., B*, 2025, **361**, 124598.

12 Z. Wu, Q. Li, G. Xu, W. Jin, W. Xiao, Z. Li, T. Ma, S. Feng and L. Wang, *Adv. Mater.*, 2024, **36**, 2311018.

13 H. Yan, C. Tian, L. Wang, A. Wu, M. Meng, L. Zhao and H. Fu, *Angew. Chem. Int. Ed.,* 2015, **54**, 6325–6329.